FERMILAB-Pub-04/161-E August 2004

arXiv:hep-ex/0406003 v1 1 Jun 2004

Measurements of Semileptonic K_L Decay Form Factors

T. Alexopoulos,[11] M. Arenton,[10] R.F. Barbosa,[7,*] A.R. Barker,[5,†] L. Bellantoni,[7] A. Bellavance,[9] E. Blucher,[4] G.J. Bock,[7] E. Cheu,[1] S. Childress,[7] R. Coleman,[7] M.D. Corcoran,[9] B. Cox,[10] A.R. Erwin,[11] R. Ford,[7] A. Glazov,[4] A. Golossanov,[10] J. Graham,[4] J. Hamm,[1] K. Hanagaki,[8] Y.B. Hsiung,[7] H. Huang,[5] V. Jejer,[10] D.A. Jensen,[7] R. Kessler,[4] H.G.E. Kobrak,[3] K. Kotera,[8] J. LaDue,[5] A. Ledovskoy,[10] P.L. McBride,[7] E. Monnier,[4,‡] H. Nguyen,[7] R. Niclasen,[5] V. Prasad,[4] X.R. Qi,[7] E.J. Ramberg,[7] R.E. Ray,[7] M. Ronquest,[10] E. Santos,[7,*] P. Shanahan,[7] J. Shields,[10] W. Slater,[2] D. Smith,[10] N. Solomey,[4] E.C. Swallow,[4,6] R.J. Tesarek,[7] P.A. Toale,[5] R. Tschirhart,[7] Y.W. Wah,[4] J. Wang,[1] H.B. White,[7] J. Whitmore,[7] M. Wilking,[5] B. Winstein,[4] R. Winston,[4] E.T. Worcester,[4] T. Yamanaka,[8] and E. D. Zimmerman[5]

(The KTeV Collaboration)

[1] *University of Arizona, Tucson, Arizona 85721*
[2] *University of California at Los Angeles, Los Angeles, California 90095*
[3] *University of California at San Diego, La Jolla, California 92093*
[4] *The Enrico Fermi Institute, The University of Chicago, Chicago, Illinois 60637*
[5] *University of Colorado, Boulder, Colorado 80309*
[6] *Elmhurst College, Elmhurst, Illinois 60126*
[7] *Fermi National Accelerator Laboratory, Batavia, Illinois 60510*
[8] *Osaka University, Toyonaka, Osaka 560-0043 Japan*
[9] *Rice University, Houston, Texas 77005*
[10] *The Department of Physics and Institute of Nuclear and Particle Physics, University of Virginia, Charlottesville, Virginia 22901*
[11] *University of Wisconsin, Madison, Wisconsin 53706*

We present new measurements of K_L semileptonic form factors using data collected in 1997 by the KTeV (E832) experiment at Fermilab. The measurements are based on 1.9 million $K_L \to \pi^\pm e^\mp \nu$ and 1.5 million $K_L \to \pi^\pm \mu^\mp \nu$ decays. For $f_+(t)$, we measure both a linear and quadratic term: $\lambda'_+ = (20.64 \pm 1.75) \times 10^{-3}$ and $\lambda''_+ = (3.20 \pm 0.69) \times 10^{-3}$. For $f_0(t)$, we find $\lambda_0 = (13.72 \pm 1.31) \times 10^{-3}$. These form factors are consistent with $K^\pm$ form factors, suggesting that isospin symmetry breaking effects are small. We use our measured values of the form factors to evaluate the decay phase space integrals, $I_K^e = 0.15350 \pm 0.00105$ and $I_K^\mu = 0.10165 \pm 0.00080$, where errors include uncertainties arising from the form factor parametrizations.

PACS numbers: 13.20.Eb

I. INTRODUCTION

Measurements of semileptonic form factors provide unique information about the dynamics of strong interactions. The form factors for the decays $K_L \to \pi^\pm e^\mp \nu$ and $K_L \to \pi^\pm \mu^\mp \nu$ also are needed to determine the decay phase space integrals, I_K^e and I_K^μ, and thus are important for measuring the Cabibbo-Kobayashi-Maskawa [1, 2] matrix element $|V_{us}|$ [3, 4]. In this paper, we report a new measurement of the semileptonic form factors based on data collected by the KTeV experiment at Fermilab.

The dependence of the semileptonic form factors on t, the four-momentum transfer to the leptons squared, was under serious experimental and theoretical study from the late 1960s to the early 1980s; the result of this effort was the precise measurement of the form factor in the decay $K_L \to \pi^\pm e^\mp \nu$ [5]. Nearly twenty years later, this form factor measurement was confirmed by CPLEAR [6] with precision comparable to the older experiments. The measurement presented in this paper provides another check of the older results with better precision.

The form factors in the decay $K_L \to \pi^\pm \mu^\mp \nu$, on the other hand, have been a long standing subject of experimental controversy [7]. The inconsistency of different experimental results leads to a large uncertainty in I_K^μ, reducing the usefulness of the $K_L \to \pi^\pm \mu^\mp \nu$ partial width in the extraction of $|V_{us}|$. The new KTeV measurement reduces the uncertainty in I_K^μ to the same level as in I_K^e. The improved precision of I_K^μ allows a sensitive test of the consistency between the phase space integrals and the ratio of semileptonic partial widths $\Gamma_{K\mu 3}/\Gamma_{Ke3}$.

This paper is organized as follows. Section II introduces the phenomenology of semileptonic form factors. Section III describes the experimental technique used to determine the form factor values. The KTeV detector, Monte Carlo simulation (MC), and data selection are described in Section IV. Section V explains the fitting procedure to extract the form factors and Section VI describes the systematic uncertainties in the analysis. Finally, in Section VII, we present results for the form factors and for the phase space integrals.

*Permanent address: University of São Paulo, São Paulo, Brazil
†Deceased.
‡Permanent address: C.P.P. Marseille/C.N.R.S., France

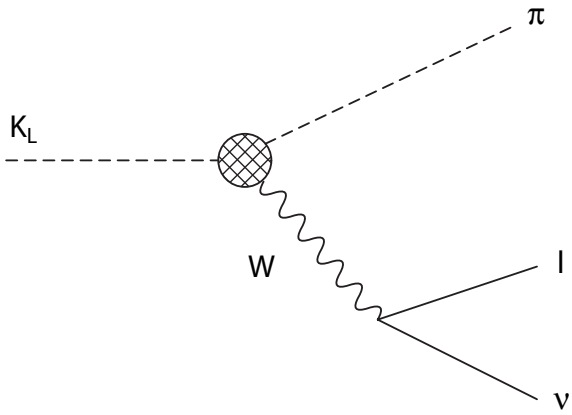

FIG. 1: Feynman diagram for the decay $K_L \to \pi^\pm \ell^\mp \nu$. The hashed circle indicates the hadronic vertex that depends on decay form factors.

II. FORM FACTOR PHENOMENOLOGY

In the Standard Model, the Born-level matrix element for the $K_L \to \pi^\pm \ell^\mp \nu$ decay modes (Fig. 1) is [32]

$$\begin{aligned}\mathcal{M} = \frac{G_F}{\sqrt{2}} V_{us} [f_+(t)(P_K + P_\pi)^\mu \overline{u_\ell} \gamma_\mu (1+\gamma_5) u_\nu \\ + f_-(t)(P_K - P_\pi)^\mu \overline{u_\ell} \gamma_\mu (1+\gamma_5) u_\nu],\end{aligned} \tag{1}$$

where G_F is the Fermi constant and f_+ and f_- are the vector form factors. Time-reversal invariance guaranties that the form factors are real, while local creation of the lepton pair requires that they be functions only of the square of the four momentum transfer to the leptons:

$$Q^2 = (P_\ell + P_\nu)^2 = (P_K - P_\pi)^2 = t \ . \tag{2}$$

The above equality holds for Born-level kinematics. For radiative $K_L \to \pi^\pm \ell^\mp \nu \gamma$ events, we assume that the form factors depend only on the virtuality of the exchange boson at the hadronic vertex [33].

f_+ and f_- are not the only possible pair of form factors that can describe semileptonic kaon decays. More recent experiments have chosen to use f_0 instead of f_-:

$$f_0(t) = f_+(t) + \frac{t}{M_K^2 - M_\pi^2} f_-(t), \tag{3}$$

where M_K and M_π are the kaon and pion mass. f_+ and f_0 correspond to the 1^- (vector) and 0^+ (scalar) exchange amplitudes, respectively. For the Born-level matrix element, f_0 is multiplied by the lepton mass M_ℓ; for $K_L \to \pi^\pm e^\mp \nu$, it is negligible compared to the contribution of f_+.

Note that for the $f_+(t)$ and $f_0(t)$ form factors, $f_+(0) = f_0(0)$; otherwise $f_-(t)$ is divergent for $t \to 0$. To simplify the notation, we use normalized form factors, $\hat{f}_{+,0}(t) = f_{+,0}(t)/f_+(0)$.

Historically, the normalized form factors $\hat{f}_+(t)$ and $\hat{f}_0(t)$ were usually analyzed assuming a linear t dependence:

$$\begin{aligned}\hat{f}_+(t) &= 1 + \lambda_+ \frac{t}{M_\pi^2} \\ \hat{f}_0(t) &= 1 + \lambda_0 \frac{t}{M_\pi^2} \ .\end{aligned} \tag{4}$$

This linear parametrization gave an adequate description of the experimental data. With a larger data sample and better control of systematic uncertainties, we study the second order term in f_+ [34]:

$$\hat{f}_+(t) = 1 + \lambda'_+ \frac{t}{M_\pi^2} + \frac{1}{2}\lambda''_+ \frac{t^2}{M_\pi^4} \ . \tag{5}$$

The presence of higher order terms is motivated by the pole model, in which the t dependence of $\hat{f}_+(t)$ and $\hat{f}_0(t)$ is described by exchange of the lightest vector and scalar K^* mesons, respectively:

$$\begin{aligned}\hat{f}_+(t) &= \frac{M_v^2}{M_v^2 - t} \\ \hat{f}_0(t) &= \frac{M_s^2}{M_s^2 - t} \ .\end{aligned} \tag{6}$$

Pole models expect $M_v \approx 892$ MeV, the mass of the lightest vector strange-meson, and $M_s > M_v$. The vector meson dominance picture is supported by the recent results on $\tau \to K\pi\nu$ decays showing a large enhancement of the $K^*(892)$ channel [8, 9, 10].

From the Born-level matrix element (Eq. 1), the $K_L \to \pi^\pm \ell^\mp \nu$ decay rate is

$$\Gamma_{K\ell 3} = \frac{G_F^2 M_K^5}{192\pi^3} S_{EW} (1 + \delta_K^\ell) \left|V_{us}\right|^2 \left|f_+^2(0)\right| I_K^\ell \ . \tag{7}$$

S_{EW} [11] is the short-distance radiative correction that is the same for both modes and $(1+\delta_K^\ell)$ [12, 13] are mode-dependent, long-distance radiative corrections. The dimensionless decay phase space integrals, I_K^ℓ, depend on the decay form factors [3]:

$$I_K^\ell = \int dt \ \frac{1}{M_K^8} \ \lambda^{3/2} \ F(t, \hat{f}_+(t), \hat{f}_0(t)) \ , \tag{8}$$

where

$$\begin{aligned}F(t, \hat{f}_+(t), \ \hat{f}_0(t)) = \left(1 + \frac{M_\ell^2}{2t}\right)\left(1 - \frac{M_\ell^2}{t}\right)^2 \times \\ \left(\hat{f}_+^2(t) + \frac{3M_\ell^2 \left(M_K^2 - M_\pi^2\right)^2}{\left(2t + M_\ell^2\right)\lambda} \ \hat{f}_0^2(t)\right)\end{aligned} \tag{9}$$

and

$$\lambda = t^2 + M_K^4 + M_\pi^4 - 2tM_K^2 - 2tM_\pi^2 - 2M_K^2 M_\pi^2 \ . \tag{10}$$

III. FORM FACTOR EXTRACTION PROCEDURE

For a semileptonic decay detected by KTeV, the kaon direction of flight is well measured, but the kaon energy is

not uniquely determined. Using the reconstructed missing transverse momentum squared associated with the neutrino ($p^2_{\perp,\nu}$) and the invariant mass of the pion-lepton system ($M_{\pi\ell}$), one can uniquely determine the square of the neutrino longitudinal momentum in the kaon rest frame:

$$P^{*}_{\parallel,\nu}{}^{2} = \frac{\left(M_K^2 - M_{\pi\ell}\right)^2}{4M_K^2} - p^2_{\perp,\nu} \ . \tag{11}$$

The sign ambiguity for $P^*_{\parallel,\nu}$ leads to a twofold ambiguity for the parent kaon energy, E_K, which in turn gives rise to two different values of t.

Most previous fixed target experiments encountered the same twofold kaon energy ambiguity. Typical solutions to this problem included selecting events with small $|P^*_{\parallel,\nu}|$, picking the more probable solution, or using both solutions with weights proportional to the probability of each solution. In these approaches, the probability of a given solution depended on the form factors and the kaon energy spectrum, which was often not well understood; this coupling increased the systematic uncertainty.

In this paper, we describe a technique to measure form factors that avoids the twofold E_K ambiguity. The key idea in this method is that instead of t, we use "transverse t," which is defined by substituting the measured transverse momenta for the full 3-momenta in Eq. 2. A similar approach was used in [14].

We introduce two definitions of transverse t following the two definitions of t. We define "lepton transverse t", $t^\ell_\perp$, by modifying $(P_\ell + P_\nu)^2$:

$$\begin{aligned} t^\ell_\perp &= M_\ell^2 + 2|p_{\perp,\nu}|\sqrt{p^2_{\perp,\ell} + M_\ell^2} - 2\mathbf{p}_{\perp,\nu}\mathbf{p}_{\perp,\ell} \\ &= M_\ell^2 + 2|p_{\perp,\nu}|\sqrt{p^2_{\perp,\ell} + M_\ell^2} + p^2_{\perp,\ell} + p^2_{\perp,\nu} - p^2_{\perp,\pi} \ . \end{aligned} \tag{12}$$

In a similar way, we define "pion transverse t," $t^\pi_\perp$, by modifying $(P_K - P_\pi)^2$:

$$t^\pi_\perp = M_K^2 + M_\pi^2 - 2M_K\sqrt{p^2_{\perp,\pi} + M_\pi^2} \ . \tag{13}$$

Note that from Eq. 2, the following inequality holds:

$$t^\ell_\perp \le t \le t^\pi_\perp \ . \tag{14}$$

To simplify the notation, we use the symbol $t_\perp$ if the discussion refers to either $t^\pi_\perp$ or $t^\ell_\perp$; the symbol $t^{\ell,\pi}_\perp$ is used to refer to both $t^\pi_\perp$ and $t^\ell_\perp$.

Since the K_L is a scalar particle, the decay kinematics does not depend on the K_L direction. Therefore, the $t_\perp$ distribution can be unambiguously related to the t distribution and vice versa. The value of $t_\perp$ is invariant under kaon boosts, and thus the $t_\perp$ distribution does not depend on the kaon energy spectrum. The loss of longitudinal information does not dramatically increase the statistical uncertainty: a MC study shows that the $t_\perp$-based measurement of the form factors leads to a 15% increase in uncertainty with respect to an ideal, t-based measurement.

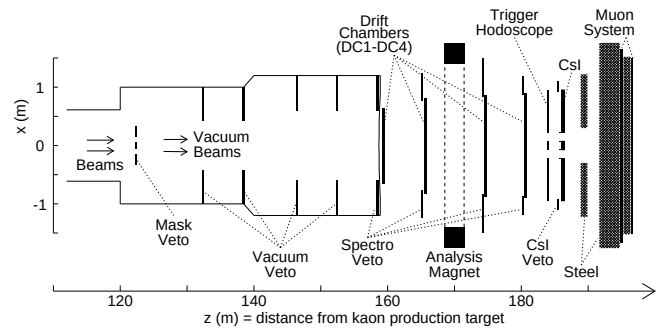

FIG. 2: Plan view of the KTeV (E832) detector. The evacuated decay volume ends with a thin vacuum window at $Z = 159$ m. The label "CsI" indicates the electromagnetic calorimeter.

Each definition of $t_\perp$ can be used to measure the form factors. We will refer to the extraction of form factors using the $t^\ell_\perp$ or $t^\pi_\perp$ variables as the $t^\ell_\perp$- or $t^\pi_\perp$-methods, respectively. The two methods have a different sensitivity to systematic effects. For example, the $t^\pi_\perp$-method is much less sensitive to radiative corrections, and therefore is used for the $K_L \to \pi^\pm e^\mp \nu$ decay mode, while the $t^\ell_\perp$-method leads to better statistical precision, and is used for the $K_L \to \pi^\pm \mu^\mp \nu$ decay mode.

The form factor measurement starts with a determination of the $t_\perp$ distribution in data. We use a Monte Carlo simulation to determine the detector acceptance as a function of $t_\perp$ and also to calculate radiative corrections. We extract the form factors by fitting the Monte Carlo simulation to data as will be described in Section V.

IV. APPARATUS, SIMULATION, AND DATA SELECTION

The KTeV experiment (Fig. 2) and associated event reconstruction techniques have been described in detail elsewhere [15]. An 800 GeV/c proton beam striking a BeO target is used to produce two almost parallel neutral beams. A large vacuum decay region surrounded by photon veto detectors extends from 110 m to 159 m from the primary target. Following a thin vacuum window at the end of the vacuum region is a drift chamber spectrometer, equipped with an analysis magnet which imparts a 0.41 GeV/c kick in the horizontal plane. Farther downstream, there is a trigger hodoscope, a pure CsI electromagnetic calorimeter, and a muon system consisting of two scintillator hodoscopes behind 4 m and 5 m of steel.

A detailed Monte Carlo simulation is used to correct for the acceptance of the $K_L \to \pi^\pm \ell^\mp \nu$ decay modes. The MC includes three main steps: event generation, propagation of particles through the detector, and simulation of the detector performance. A thorough discussion of this simulation program is given in [15], and more specifically for $K_L \to \pi^\pm \ell^\mp \nu$ decays in [16]. To include leading-

order QED radiative corrections, we use the KLOR program [13].

For this analysis, we use a low intensity data sample collected in 1997, which is the same data sample used to measure $\Gamma(K_L \to \pi^\pm\mu^\mp\nu)/\Gamma(K_L \to \pi^\pm e^\mp\nu)$ [16]. Consequently, most of the data selection requirements are similar to those used in the KTeV partial width ratio analysis.

The reconstruction begins with the identification of two oppositely charged tracks coming from a single vertex, reconstructed between 123 and 158 m from the primary target. To pass the event selection, one of the two tracks must be within 7 cm of a cluster in the CsI calorimeter; the second track is not required to have a cluster match. The event's missing transverse momentum squared associated with the neutrino is calculated with respect to the line connecting the primary target and the decay vertex. Both kaon energy solutions are required to fall between 40 and 120 GeV, where the kaon momentum spectrum is well measured.

The decay $K_L \to \pi^\pm e^\mp\nu$ is identified using E/p, the energy reconstructed in the CsI calorimeter divided by the momentum measured in the spectrometer. One track is required to have E/p greater than 0.92 and the other track is required to have E/p less than 0.85. The first condition is satisfied for 99.8% of electrons and failed by 99.5% of pions. The second condition is satisfied for 99.1% of pions and failed by 99.93% of electrons. The resulting unambiguous identification of the pion and electron in the decay $K_L \to \pi^\pm e^\mp\nu$ (swap probability $< 0.01\%$) allows for the correct reconstruction of $t_\perp$.

The decay $K_L \to \pi^\pm\mu^\mp\nu$ is identified by requiring one of the tracks to have an energy deposit in the CsI less than 2 GeV [35], and the other track to have E/p less than 0.85. This selection strongly suppresses $K_L \to \pi^\pm e^\mp\nu$ decays; however, since the CsI calorimeter is only about 1/3 of a hadronic interaction length, the calorimeter selection is not very effective in reducing background from $K_L \to \pi^+\pi^-\pi^0$ and $K_L \to \pi^+\pi^-$.

In both semileptonic decay modes, $K_L \to \pi^+\pi^-\pi^0$ background is rejected using the variable k_{+-0} [16]. For a genuine $K_L \to \pi^+\pi^-\pi^0$ event, k_{+-0} is proportional to the square of the π^0 longitudinal momentum in the reference frame in which the sum of π^+-π^- momenta is orthogonal to the kaon direction. We require $k_{+-0} < -0.006$, rejecting 99.9% of $K_L \to \pi^+\pi^-\pi^0$ decays while retaining 99.5% of $K_L \to \pi^\pm e^\mp\nu$ and 97.9% of $K_L \to \pi^\pm\mu^\mp\nu$ decays. $K_L \to \pi^+\pi^-$ background is suppressed by rejecting events in which the two-track invariant mass, assuming both tracks are pions, is between 0.488 and 0.505 GeV/c^2.

The main difference in the selection of the decay $K_L \to \pi^\pm\mu^\mp\nu$ compared to the partial width ratio analysis is driven by the need to distinguish between the pion and muon tracks in order to reconstruct $t_\perp$. Since the calorimeter selection does not uniquely identify the pion and muon, we identify the muon by requiring the extrapolation of a track to be near fired horizontal and vertical counters in the muon system. The quality of this "match" is measured by a χ^2_μ variable that accounts for momentum-dependent multiple scattering in the steel in front of the muon system. We reject events with two matched tracks to suppress muon misidentification from $\pi \to \mu\nu$ decays and from pion penetrations through the steel. The misidentification is suppressed further by requiring 0.5 m separation between the two tracks at the muon system (compared to the 0.15 m segmentation of the muon system counters). The efficiency of the matching requirement is increased by demanding that the muon track projection be at least 0.25 m inside the muon system outer aperture. To reduce the fraction of muons ranging out in the steel, we also require that the muon track momentum be greater than 10 GeV. These selection criteria result in the unambiguous identification of the pion and muon in the decay $K_L \to \pi^\pm\mu^\mp\nu$, with a swap probability of less than 0.1%.

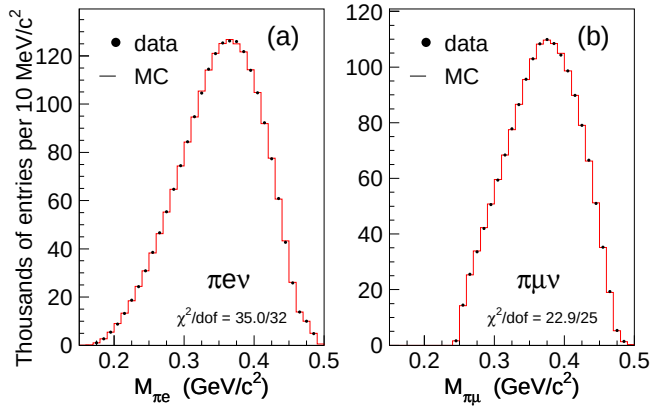

FIG. 3: The invariant mass distribution (a) $M_{\pi e}$ for $K_L \to \pi^\pm e^\mp\nu$ events and (b) $M_{\pi\mu}$ for $K_L \to \pi^\pm\mu^\mp\nu$ events. Data are shown as dots; MC is shown as a histogram. All analysis requirements have been applied.

There are two categories of background in this analysis: misidentified kaon decays and scattering background caused by a kaon scattering off a beamline element (absorber or collimator). The misidentification background for the $K_L \to \pi^\pm e^\mp\nu$ decay mode is below 10^{-5} and is ignored. The background for the $K_L \to \pi^\pm\mu^\mp\nu$ decay mode is also small (10^{-4}), but is not uniform in $t_\perp^{\ell,\pi}$ and must be subtracted. Kaon scattering off beamline elements, resulting in an incorrect measurement of $p_\perp^2$, affects $(0.11 \pm 0.01)\%$ of all events. Systematic uncertainties arising from the modeling of the background are discussed in Section VI C.

The main kinematic variables for the extraction of the semileptonic form factors are the transverse momenta-squared of all three particles, $p^2_{\perp,\nu}$, $p^2_{\perp,\ell}$ and $p^2_{\perp,\pi}$, as well as the pion-lepton invariant mass, $M_{\pi\ell}$. Distributions of $M_{\pi\ell}$ for the $K_L \to \pi^\pm e^\mp\nu$ and $K_L \to \pi^\pm\mu^\mp\nu$ decay modes are shown in Figure 3. Distributions of $p^2_{\perp,\nu}$, $p^2_{\perp,\ell}$ and $p^2_{\perp,\pi}$ are shown in Figure 4.

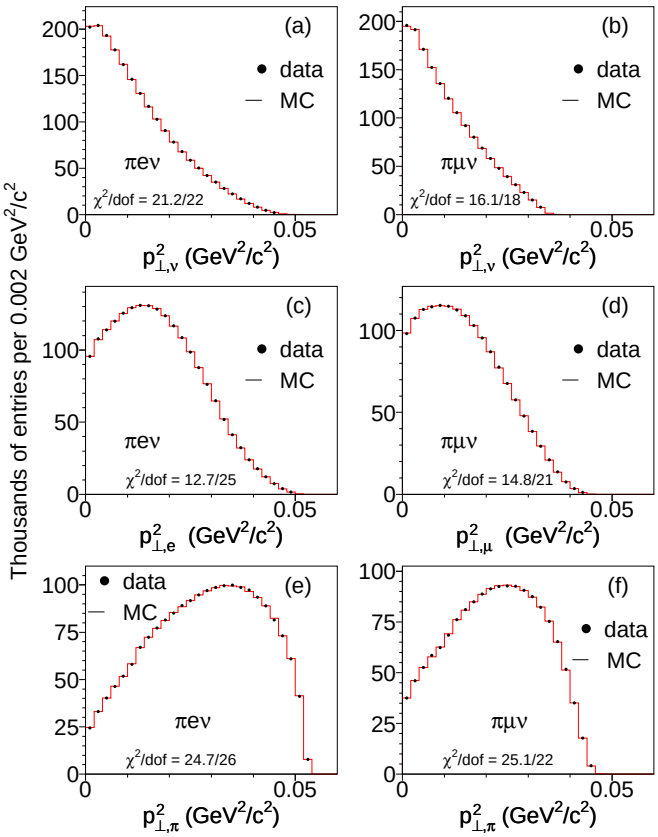

FIG. 4: Distribution of (a) $p^2_{\perp,\nu}$ for $K_L \to \pi^\pm e^\mp \nu$ events, (b) $p^2_{\perp,\nu}$ for $K_L \to \pi^\pm \mu^\mp \nu$ events, (c) $p^2_{\perp,e}$ for $K_L \to \pi^\pm e^\mp \nu$ events, (d) $p^2_{\perp,\mu}$ for $K_L \to \pi^\pm \mu^\mp \nu$ events, (e) $p^2_{\perp,\pi}$ for $K_L \to \pi^\pm e^\mp \nu$ events, and (f) $p^2_{\perp,\pi}$ for $K_L \to \pi^\pm \mu^\mp \nu$ events (d). Data are shown as dots, signal MC is shown as histogram. All analysis requirements have been applied.

Note that the $M_{\pi\ell}$ and $p^2_\perp$ distributions (Figs. 3,4) have different sensitivity to radiative effects and form factor values. For example, using the $K_L \to \pi^\pm e^\mp \nu$ MC without radiative effects, the form factor obtained with the $t^\pi_\perp$-method gives good data-MC agreement in $p^2_{\perp,\pi}$, but poor agreement in the $M_{\pi e}$ and $p^2_{\perp,e}$ distributions. Conversely, the form factor obtained with the $t^\ell_\perp$-method gives good data-MC agreement in $M_{\pi e}$ and $p^2_{\perp,e}$, but poor agreement in $p^2_{\perp,\pi}$. The excellent data-MC agreement shown in all four distributions ($M_{\pi e}$, $p^2_{\perp,\nu}$, $p^2_{\perp,e}$ and $p^2_{\perp,\pi}$ in Figs. 3,4) is possible only if radiative effects are included in the MC.

The measurement of the semileptonic form factors benefits greatly from the excellent resolution of the KTeV spectrometer ($< 1\%$), and also from the extensive calibration performed for the measurement of ϵ'/ϵ [15]. The resulting $t_\perp$ resolution is better than 1.5% on average.

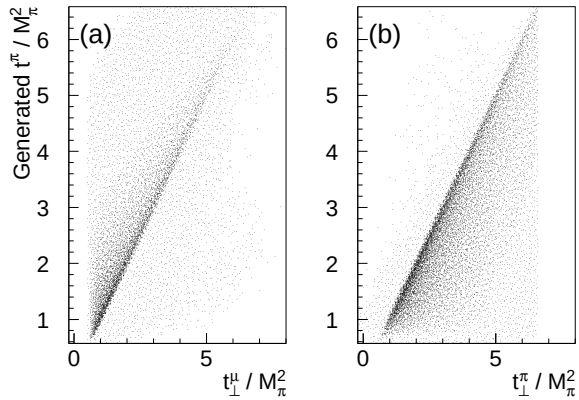

FIG. 5: The distribution of generated t^π versus reconstructed $t_\perp$, which is used to construct the matrix $\mathcal{A}_{rg}$, for (a) $t^\mu_\perp$-method and (b) $t^\pi_\perp$-method. The plot is based on the $K_L \to \pi^\pm \mu^\mp \nu$ decay mode.

V. FITTING

We employ two different strategies to extract the form factors from the measured $t_\perp$ distribution. In the first method ("fit-A"), we use the MC to obtain the matrix $\mathcal{A}_{rg}$, which relates the generated $t^\pi = (P_K - P_\pi)^2$, g-index, to the reconstructed $t^\ell_\perp$ or $t^\pi_\perp$, r-index. Note that detector resolution and radiative effects are included in this matrix. Figure 5 shows the distribution of t^π and $t^{\ell,\pi}_\perp$ that is used to calculate the matrix $\mathcal{A}_{rg}$ [36].

Using the matrix $\mathcal{A}_{rg}$, we construct the prediction for the binned distribution of the reconstructed $t_\perp$:

$$\mathcal{N}^{predA}_{\perp,r} = N_0 \sum_g \mathcal{A}_{rg} \frac{F(t_g, \hat{f}^{pred}_+(t_g), \hat{f}^{pred}_0(t_g))}{F(t_g, \hat{f}^{MC}_+(t_g), \hat{f}^{MC}_0(t_g))}. \quad (15)$$

Here, $F(t, \hat{f}_+(t), \hat{f}_0(t))$ is the Born-level t distribution function (Eq. 9) which depends on the form factors [37]; $\hat{f}^{MC}_{+,0}$ are the form factors used in MC and $\hat{f}^{pred}_{+,0}$ are the form factors floated in the fit; t_g are the bin centers and N_0 is the overall normalization, which is also floated in the fit. For $\hat{f}^{pred}_{+,0} = \hat{f}^{MC}_{+,0}$, the prediction $\mathcal{N}^{predA}_{\perp,r}$ is simply the reconstructed $t_\perp$ distribution from MC. For different $\hat{f}^{pred}_{+,0}$, the prediction function (Eq. 15) is equivalent to "reweighting" the MC to the new values of the form factors. The actual fit is the χ^2 minimization between the binned $t_\perp$ distribution in data and the prediction $\mathcal{N}^{predA}_{\perp,r}$.

In the second method ("fit-B"), we follow a common approach in which we fit the data $t_\perp$ distribution, corrected for acceptance and radiative effects, to the Born-level prediction. First, we define the acceptance A_b in a given bin of $t^{\ell,\pi}_{\perp,b}$ as the ratio of the number of reconstructed events to the number of generated events in the bin. Next, we define the radiative correction $(1 + \delta_b)$ for each bin as the ratio of the number of generated events for the nominal MC (including radiative effects from KLOR)

to the number of generated events for a separate Born-level MC; these MC samples are normalized using the global radiative correction $(1+\delta_K^\ell)$. After correcting for acceptance and radiative effects, the number of corrected data events for a given $t_\perp$ bin is given by

$$N_{\perp,b}^{Born} = \frac{N_{\perp,b}^{rec}}{A_b(1+\delta_b)} \ , \tag{16}$$

where $N_{\perp,b}^{rec}$ is the number of reconstructed events. Both acceptance and radiative corrections depend on the form factors and are therefore determined in an iterative procedure starting with the PDG values. Since this form factor dependence is relatively weak, only one iteration is required for convergence.

To determine the prediction for the Born-level $t_\perp$ distribution, we start with a quadratic parametrization of the form factors (Eq. 5). We square the matrix element (Eq. 1) and collect terms proportional to $\lambda'_+, {\lambda'_+}^2, \lambda''_+, {\lambda''_+}^2$, $\lambda'_0, {\lambda'_0}^2, \lambda''_0, {\lambda''_0}^2$, and cross terms. As a result, $|\mathcal{M}|^2$ may be expressed as a second order function of $\lambda'_+, \lambda'_0, \lambda''_+, \lambda''_0$:

$$|\mathcal{M}|^2 = \mathcal{I} + \lambda'_+ \mathcal{I}^{+'} + \lambda'_0 \mathcal{I}^{0'} + ... \ , \tag{17}$$

where $\mathcal{I}$ are functions of the Dalitz plot variables. We generate $K_L \to \pi^\pm e^\mp \nu$ and $K_L \to \pi^\pm \mu^\mp \nu$ decays according to three-body phase space kinematics and numerically integrate over $\mathcal{I}$ for events falling into the same $t_\perp$ bin. In this way, the prediction for the binned $t_\perp$ distribution can be expressed as

$$\mathcal{N}_{\perp,b}^{predB}(\lambda'_+, \lambda'_0, ...) = \mathcal{I}_{\perp,b} + \lambda'_+ \mathcal{I}_{\perp,b}^{+'} + \lambda'_0 \mathcal{I}_{\perp,b}^{0'} + ... \ , \tag{18}$$

where $\mathcal{I}_{\perp,b}$ are the results of the integration explained above. For the pole model fit, we first Taylor expand the pole parametrization (Eq. 6) up to second order in t to obtain

$$\lambda'_+ = \frac{M_\pi^2}{M_v^2} \ \text{ and } \ \lambda''_+ = 2\frac{M_\pi^4}{M_v^4} \tag{19}$$

(and similar expressions for λ'_0 and λ''_0 as a function of M_s), and then use the prediction given by Eq. 18.

The ratios $\lambda_+ \mathcal{I}_{\perp,b}^+ / \mathcal{I}_{\perp,b}$ and $\lambda_0 \mathcal{I}_{\perp,b}^0 / \mathcal{I}_{\perp,b}$ govern the influence of the λ_+ and λ_0 parameters on the $t_\perp^{\ell,\pi}$ distributions. These ratios are illustrated in Figure 6 for typical values of λ_+ and λ_0. In a similar manner, we determine the influence of λ_+ and λ_0 on the $M_{\pi\mu}$ distribution for the $K_L \to \pi^\pm \mu^\mp \nu$ decay mode (Figure 6 (c)). For the decay $K_L \to \pi^\pm e^\mp \nu$, $\lambda_+ = 0.03$ corresponds to a linear increase of the decay rate as a function of $t_\perp^\ell$; for $t_\perp^\ell / M_{\pi^2} = 6$, this increase is about 40%. For $K_L \to \pi^\pm \mu^\mp \nu$, the effect of λ_0 is non-linear and is more pronounced for large $t_\perp^\ell$ and small $m_{\pi\mu}^2$.

The advantage of fit-A is that there is no need for an iterative determination of the acceptance since the method is almost independent of the form factors used in the MC. The matrix $\mathcal{A}_{rg}$ also utilizes the detector resolution information, which leads to better statistical precision compared to fit-B (by about 10%). On the other hand, the advantage of fit-B is an easy generalization to 2-dimensional fits, in particular to fit in $(M_{\pi\ell}, t_\perp)$ space. Although fit-B has less precision than fit-A for 1-dimensional fits, the precision is improved in 2-dimensional fits by using the different shapes of the λ_0 and λ_+ distributions as a function of $m_{\pi\mu}^2$ (Fig. 6 (c)).

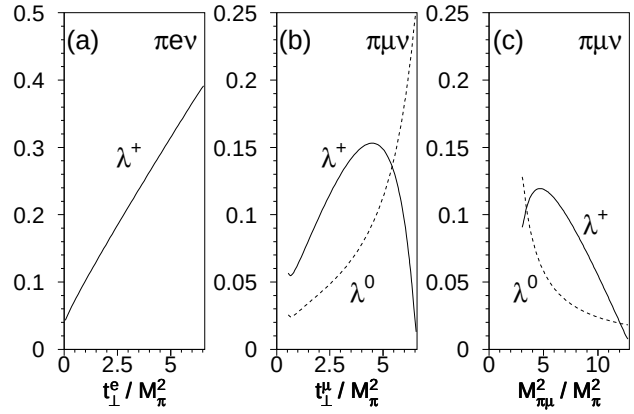

FIG. 6: Illustration of the influence of the form factors $\lambda_+ = 0.03$ and $\lambda_0 = 0.02$ on the $t_\perp^\ell$ and $M_{\pi\mu}$ distributions. The figure shows $0.03 \times \mathcal{I}_{\perp,b}^{+'}/\mathcal{I}_{\perp,b}$ (solid lines marked as "λ_+") and $0.02 \times \mathcal{I}_{\perp,b}^{0'}/\mathcal{I}_{\perp,b}$ (dashed lines marked as "λ_0") (a) as a function of $t_\perp^e$ for decay $K_L \to \pi^\pm e^\mp \nu$, (b) as a function of $t_\perp^\mu$ for decay $K_L \to \pi^\pm \mu^\mp \nu$, and (c) as a function of $M_{\pi\mu}$ for decay $K_L \to \pi^\pm \mu^\mp \nu$.

Both fitting methods are checked using MC samples generated with different values of form factors. The estimation of the statistical uncertainty is verified by generating 100 independent MC samples and studying the distribution of the fitted form factors. For the one dimensional fits in $t_\perp$, the form factors for $K_L \to \pi^\pm e^\mp \nu$ and $K_L \to \pi^\pm \mu^\mp \nu$ are extracted using both fitting techniques; these measurements are consistent within the uncorrelated statistical uncertainty.

VI. SYSTEMATIC UNCERTAINTIES

The sources of systematic uncertainty for this analysis are the same as for the partial width ratio measurements [16], but their impact on the result is different. The form factor measurement does not depend on uniform losses that do not bias kinematic distributions. For example, losses caused by hadronic interactions inside the spectrometer have virtually no influence. On the other hand, effects that cause misreconstruction of event kinematics, such as calibration of the analysis magnet kick, are more significant.

Table I summarizes the systematic uncertainties for the form factor measurements. For each decay mode and for each type of parametrization, the uncertainties are

evaluated for the results obtained using both the $t_\perp^\pi$ and $t_\perp^\ell$ methods. For the nominal KTeV result, we select the method which leads to the smallest total error and use the other method as a crosscheck. The nominal form factor result for $K_L \to \pi^\pm e^\mp \nu$ is based on a 1-dimensional fit to the $t_\perp^\pi$ distribution; the nominal form factor result for $K_L \to \pi^\pm \mu^\mp \nu$ is based on a 2-dimensional fit to the ($M_{\pi\mu}$,$t_\perp^\ell$) distribution.

The systematic uncertainty in the form factor resulting from a given effect is evaluated by turning this effect off in the MC simulation and determining the corresponding change in the form factors. The systematic uncertainty in the form factor is taken as this change times the relative uncertainty of the systematic effect. For example, turning off muon scattering in the steel changes λ_0 by 1.5×10^{-3}; since we model the effects of scattering with 20% precision (Sec. VI B 2), the corresponding uncertainty on λ_0 is 0.3×10^{-3}.

The following sections discuss systematic uncertainties in the order given in Table I.

A. Calibration & Alignment

1. Drift chamber alignment

The dimensions of the drift chambers are known to 20 μm from optical survey. The chamber locations along the kaon beam (z-direction) were monitored during the run and are known to 100 μm. In the transverse directions, the chambers are aligned in-situ using dedicated muon runs with the analysis magnet turned off. The transverse position of the primary target is known to 50 μm precision by projecting the total momentum of $K_L \to \pi^+\pi^-$ events to $Z = 0$.

The alignment in the horizontal direction is most important because it affects the track momentum measurement. The residual uncertainty in the alignment procedure is 20 μm. The systematic uncertainty reported in Table I is based on the sum in quadrature of the form factor changes if DC1 is shifted horizontally by 20 μm, rotated in the XY plane by 20 μrad, has non-orthogonality between vertical and horizontal wires of 50 μrad, or is shifted in Z by 100 μm.

2. Magnet Kick Calibration

The calibration of the analysis magnet transverse kick is performed with $K_L \to \pi^+\pi^-$ decays. The 30 keV uncertainty in the PDG value of M_K leads to a 0.01% uncertainty in the transverse kick.

B. Detector Simulation

1. Multiple Scattering and Resolution

As explained in [16], the amount of detector material and the influence of electromagnetic interactions (multiple scattering, bremsstrahlung and δ-ray production) on the detector acceptance are described to 10%. For the systematic uncertainty arising from modeling of the drift chamber position resolution, we assume a 5% uncertainty for the Gaussian part of the chamber response and a 10% uncertainty for the non-Gaussian tail induced by the discrete statistics of the ionization process. This estimate is based on a data-MC comparison of the distance between the track and reconstructed hits. The chamber inefficiency caused by early accidental activity as well as hadronic interactions are negligible for this analysis.

2. Muon System Simulation

Several effects must be simulated to reproduce the efficiency of the muon system. These effects are muon scattering in the steel, modeling of the cracks between the muon system counters, and pion penetrations through the steel.

Multiple scattering in the steel is modeled using a parametrization of a GEANT simulation [17]. It is checked with muons from $K_L \to \pi^\pm \mu^\mp \nu$ decays, in which the pion is unambiguously identified by requiring a hadronic shower in the CsI calorimeter [38]. Figure 7 shows the inefficiency of the muon match as a function of the muon momentum. From the distribution of distances between extrapolated muon tracks and hit muon counters, we conclude that scattering in the steel is described to better than 20% precision. The size of the cracks between the muon system counters ($\sim$ 1 mm) is determined to 50% precision using the muon runs.

The probability that a pion penetrates through the steel and leaves a signal in the muon system is measured in data using pions from fully reconstructed $K_L \to \pi^+\pi^-\pi^0$ decays. This effect is included in the MC, and is checked for $K_L \to \pi^\pm \mu^\mp \nu$ decays by studying the fraction of events in which both tracks match to hit muon system counters. For data and MC we observe matches for both tracks in 2.17% and 2.25% of the cases, respectively. According to the MC, events with two matches result from pion decays ($\sim$ 85%), pion penetrations ($\sim$ 10%) and accidental hits ($\sim$ 5%). This study shows that the combined effect of pion penetrations and decays is modeled to better than 10%.

3. Cut Variation

We have modified various selection criteria to check the stability of the measured form factors. The general strategy is to relax or tighten one requirement at a time while

TABLE I: Systematic, statistical and total uncertainties for the form factors.

Source	K_{e3} λ_+	λ_+'	λ_+"	M_v MeV	$K_{\mu3}$ λ_+	λ_0	λ_+'	λ_+"	λ_0	M_v MeV	M_s MeV
	$\times10^{-3}$				$\times10^{-3}$						
Calibration & Alignment											
- Drift Chamber Alignment	0.0	0.2	0.1	0.	0.3	0.2	0.5	0.2	0.2	5.	6.
- $P_\perp$ Kick Calibration	0.2	1.0	0.3	2.	0.2	0.3	0.0	0.1	0.4	3.	9.
Detector Simulation											
- Multiple Scattering and Resolution	0.1	0.5	0.1	2.	0.0	0.1	0.3	0.1	0.1	0.	2.
- Muon System Simulation	0.0	0.0	0.0	0.	0.1	0.3	0.3	0.1	0.3	2.	9.
- Cut Variations	0.2	0.3	0.1	1.	0.2	0.3	0.5	0.2	0.3	4.	11.
- Beam Shape and Kaon Energy Spectrum	0.1	0.0	0.0	0.	0.0	0.0	0.0	0.0	0.0	0.	0.
Background											
- Scattering Background	0.0	0.0	0.0	0.	0.0	0.0	0.0	0.0	0.0	0.	0.
- Misidentification Background	0.0	0.0	0.0	0.	0.1	0.1	0.4	0.1	0.0	2.	3.
Fitting	0.1	0.2	0.1	1.	0.2	0.2	0.4	0.3	0.2	3.	10.
Radiative Corrections	0.1	0.0	0.1	2.	0.2	0.7	0.7	0.2	0.9	3.	20.
Monte Carlo statistics	0.22	0.80	0.33	2.96	0.35	0.31	1.28	0.52	0.55	5.14	11.34
Total systematic	0.43	1.43	0.53	4.94	0.63	0.98	1.77	0.72	1.22	9.92	31.04
Data statistics	0.37	1.37	0.57	5.12	0.88	0.78	3.19	1.31	1.36	12.81	28.30
Total uncertainty	0.57	1.99	0.78	7.11	1.08	1.25	3.65	1.49	1.83	16.20	42.00

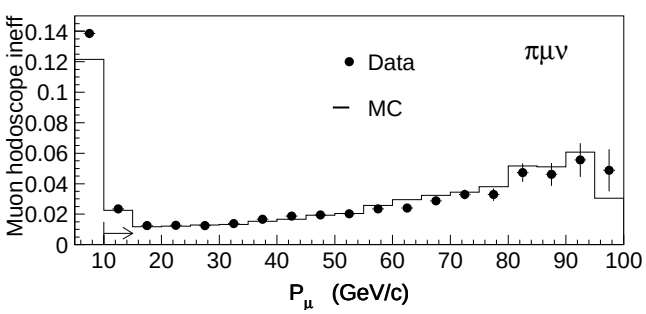

FIG. 7: Inefficiency of the muon hodoscope matching requirement as a function of the muon momentum measured with $K_L \to \pi^\pm\mu^\mp\nu$ decays. Arrow indicates the momentum requirement. The inefficiency increases with momentum because of the χ^2_μ definition.

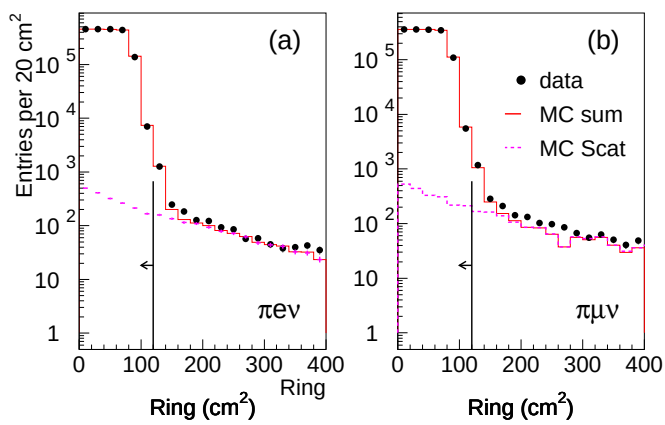

FIG. 8: Ring distributions for (a) $K_L \to \pi^\pm e^\mp\nu$, and (b) $K_L \to \pi^\pm\mu^\mp\nu$ decay mode. Dots show data, "MC sum" refers to signal plus background MC, and "MC Scat" shows the contribution from kaon scattering. The arrow indicates the analysis requirement. Events in the tail are mostly from kaon scattering.

retaining all other cuts. These requirements include the track separation requirement at the drift chambers and other fiducial and kinematic cuts.

Tests leading to significant changes are added to the systematic uncertainty. For example, an extra requirement of no photon-like clusters reconstructed in the CsI calorimeter for the $K_L \to \pi^\pm e^\mp\nu$ decay mode leads to a $(-0.13\pm0.07)\times10^{-3}$ change in λ_+, which is included as a systematic uncertainty. The systematic uncertainties in the form factors are estimated as the sum in quadrature of these variations.

4. *Beam Shape and Kaon Energy Spectrum*

The transverse shape of the kaon beam is defined by a system of collimating elements, the most important of which is the defining collimator located 88 m from the primary target. While the geometry of the defining collimator is well known, its exact alignment is harder to determine, leading to an uncertainty in the beam shape near the beam edge. The beam shape is studied using a "`RING`" variable, which is calculated using the X-Y vertex position projected along the kaon direction of flight to the calorimeter surface [15]. Figure 8 compares data and MC `RING` distributions for the two semileptonic modes. A `RING` value of 0 cm^2 corresponds to the beam center and a `RING` value of $\sim$ 100 cm^2 corresponds to the beam edge; the beam size at the calorimeter is about 10×10 cm^2.

In this analysis, we select events with `RING` < 121 cm^2.

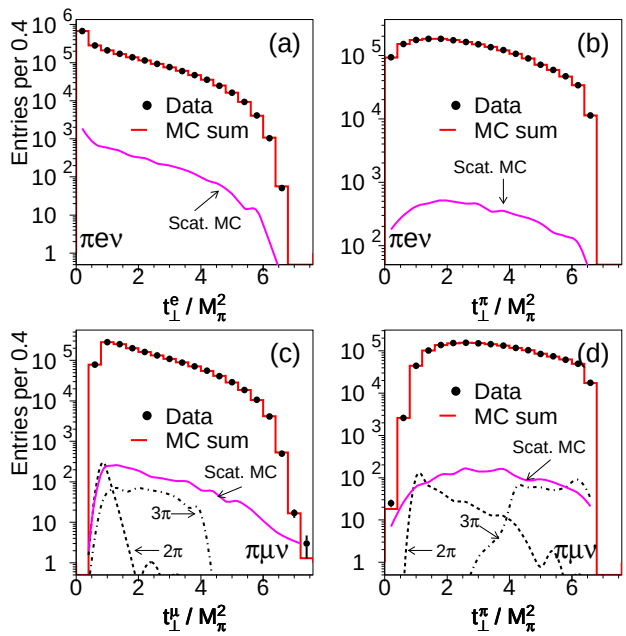

FIG. 9: Distributions for data, background MC and sum of background and signal MC for (a) $t_\perp^e/M_\pi^2$ in $K_L \to \pi^\pm e^\mp \nu$ decay mode, (b) $t_\perp^\pi/M_\pi^2$ in $K_L \to \pi^\pm e^\mp \nu$ decay mode, (c) $t_\perp^\mu/M_\pi^2$ in $K_L \to \pi^\pm \mu^\mp \nu$ decay mode, and (d) $t_\perp^\pi/M_\pi^2$ in $K_L \to \pi^\pm \mu^\mp \nu$ decay mode.

Larger RING values result mostly from kaon scattering in the defining collimator. To check if the beam edge affects the form factor measurement, we repeat the analysis with RING < 70 cm^2 and also with RING < 200 cm^2. There is no statistically significant change in the form factors, so no systematic uncertainty is assigned.

For kaon energies between 40 and 120 GeV, the kaon momentum spectrum is known to 0.01% per GeV [16]. To estimate the impact of this uncertainty on the form factor measurement, we modify the MC energy spectrum linearly within this uncertainty.

C. Background

The fraction of events in which the parent kaon has scattered in the defining collimator, as well as the shape of the resulting $p_{\perp,K}^2$ distribution, are measured with fully reconstructed $K_L \to \pi^+\pi^-\pi^0$ decays. The description of scattering is checked using events reconstructed in the sidebands of the ring number distribution (Fig. 8); this comparison shows that the level of scattering is correct to better than 10%.

The misreconstruction background in the $K_L \to \pi^\pm \mu^\mp \nu$ decay mode is from $K_L \to \pi^\pm e^\mp \nu$, $K_L \to \pi^+\pi^-\pi^0$ and $K_L \to \pi^+\pi^-$ decays. This background is determined using the MC normalized with our branching fractions [16], and is then subtracted. While this background is small, it is not uniform in $t_\perp$.

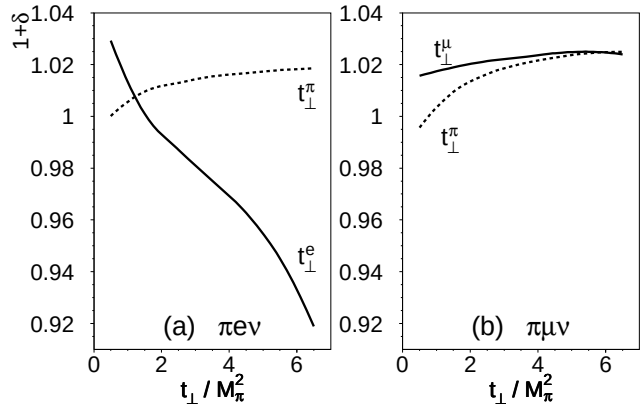

FIG. 10: Radiative correction $1+\delta = \sigma_{rad}/\sigma_{Born}$, calculated as a function of (a) $t_\perp^e/M_\pi^2$ and $t_\perp^\pi/M_\pi^2$ for $K_L \to \pi^\pm e^\mp \nu$, and (b) $t_\perp^\mu/M_\pi^2$ and $t_\perp^\pi/M_\pi^2$ for $K_L \to \pi^\pm \mu^\mp \nu$.

Figure 9 shows $t_\perp^\ell$ and $t_\perp^\pi$ distributions for the data, signal, and background MC. The systematic uncertainty in the form factors is assigned as 100% of the change if the misreconstruction background is not subtracted from the data.

D. Fitting

We study the systematic uncertainty arising in the fitting procedure by comparing fit-A with fit-B and by varying bin sizes. The results obtained with the fit-A and fit-B agree with each other within the uncorrelated statistical uncertainty.

To evaluate the systematic uncertainty caused by changes in binning, we start with the two dimensional fit-B and vary the number of bins. The number of $M_{\pi\ell}$ bins is varied between 1 and 130, and the number of $t_\perp$ bins is varied between 1 and 80. Altogether, we consider about 60 fits between these extremes. Using the deviation of each fit from the nominal fit, and the uncorrelated statistical uncertainties, we construct a χ^2_{bin}, summing over all 60 fits. We evaluate this χ^2_{bin} for all fit parameterizations. For example, λ_+ determined in the linear model fit to $K_L \to \pi^\pm e^\mp \nu$ has $\chi^2_{bin}/dof = 71.5/61$, and λ_0 determined in the linear model fit to $K_L \to \pi^\pm \mu^\mp \nu$ has $\chi^2_{bin}/dof = 85.9/60$.

To account for the observed non-statistical change of the fit results with binning changes, indicated by $\chi^2_{bin}/dof > 1$, we assign an additional systematic error. The size of this uncertainty is determined such that addition of this error (in quadrature) to the uncorrelated statistical uncertainty of each fit leads to $\chi^2_{bin}/dof = 1$.

E. Radiative corrections

Figure 10 shows the influence of radiative corrections on the $t_\perp^{\ell,\pi}$ distributions for the $K_L \to \pi^\pm \ell^\mp \nu$ decay modes. Using the $t_\perp^\ell$-method, radiative corrections are significantly larger for $K_L \to \pi^\pm e^\mp \nu$ than for $K_L \to \pi^\pm \mu^\mp \nu$; using the $t_\perp^\pi$-method, radiative corrections are similar in both decay modes.

For the $K_L \to \pi^\pm e^\mp \nu$ decay mode, variables that are based on lepton kinematics have much larger radiative corrections than variables based on pion kinematics. Consequently, the $t_\perp^\ell$-method has much greater sensitivity to radiative corrections than the $t_\perp^\pi$-method. For the $t_\perp^\ell$-method, the difference in λ_+ measured with the nominal MC compared to a MC without radiative effects is 8×10^{-3}; for the $t_\perp^\pi$-method, the corresponding difference is only 1×10^{-3}. Using the nominal MC, the agreement between the form factor values obtained using the $t_\perp^\ell$ and $t_\perp^\pi$ methods, $\Delta\lambda_+ < 0.5 \times 10^{-3}$ at 68% *c.l.* (Sec. VII C), shows that radiative corrections for the $K_L \to \pi^\pm e^\mp \nu$ decay mode are described to better than 10%.

For the $K_L \to \pi^\pm \mu^\mp \nu$ decay mode, a sensitive check of radiative corrections is achieved by comparing λ_0 measured from the $t_\perp^\ell$ and $M_{\pi\mu}$ distributions in separate 1-dimensional fits. For our MC without radiative effects, the two fits return λ_0 values that are different by $\Delta\lambda_0 = (6.5 \pm 1.3) \times 10^{-3}$, while the nominal MC gives good agreement: $\Delta\lambda_0 = (-0.1 \pm 1.3) \times 10^{-3}$. This agreement shows that radiative corrections for the $K_L \to \pi^\pm \mu^\mp \nu$ decay mode are described to better than 20% precision.

F. Summary of Systematic Uncertainties

The total systematic uncertainty in the form factors is calculated as the sum of systematic uncertainties in quadrature (Table I). For λ_+ measured in the $K_L \to \pi^\pm e^\mp \nu$ decay mode, there are comparable contributions to the uncertainty from magnet kick calibration, cut variation, and multiple scattering and resolution effects. For λ_0 measured in the $K_L \to \pi^\pm \mu^\mp \nu$ decay mode, the largest systematic uncertainty is from modeling radiative corrections in the MC; this uncertainty is limited by the statistical uncertainty of the test described in Sec. VI E.

VII. RESULTS

A. Form Factor results

After all selection cuts and background subtraction, we have 1950543 $K_L \to \pi^\pm e^\mp \nu$ and 1535951 $K_L \to \pi^\pm \mu^\mp \nu$ decays, respectively. Using these data, we extract $\hat{f}_+(t)$ in the $K_L \to \pi^\pm e^\mp \nu$ decay mode, and both $\hat{f}_+(t)$ and $\hat{f}_0(t)$ in the $K_L \to \pi^\pm \mu^\mp \nu$ decay mode. For the nom-

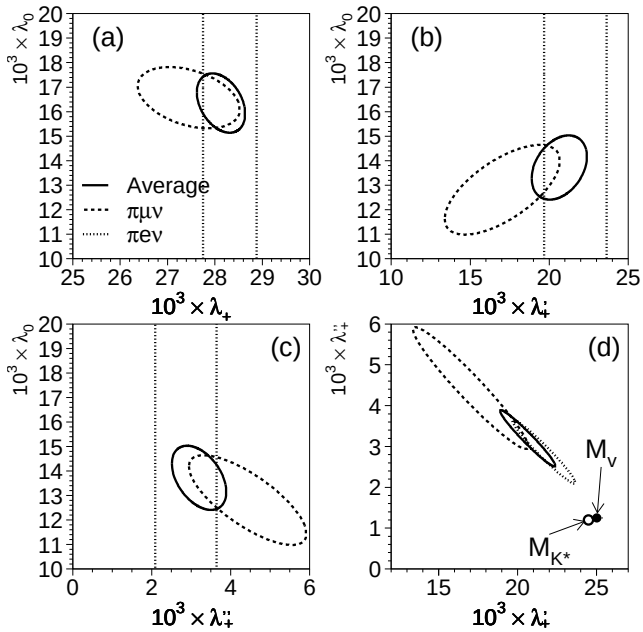

FIG. 11: 1σ correlation contours for the (a) linear fit between λ_0 and λ_+, (b) quadratic fit between λ_0 and λ'_+, (c) quadratic fit between λ_0 and λ''_+, and (d) quadratic fit between λ''_+ and λ'_+. The dotted curve is for $K_L \to \pi^\pm e^\mp \nu$ only, the dashed curve is for $K_L \to \pi^\pm \mu^\mp \nu$ only, and the solid curve is for the average of the two decay modes. The open and closed circle in (d) represents λ'_+, λ''_+ obtained from the Taylor expansion of the pole parametrization (Eq. 19) around M_{K^*} and around M_v, respectively.

TABLE II: Form factor results for both $K_L \to \pi^\pm \ell^\mp \nu$ decay modes and the average measured for Linear, Quadratic and Pole mode parametrization. The uncertainties correspond to the total uncertainties; the breakdown into statistical and systematic uncertainty is given in Table I. The correlation coefficients between the form factors are given in Table III. χ^2/ndf for individual modes correspond to statistical uncertainty only; χ^2/ndf for the average includes uncorrelated systematic uncertainty. See text for explanation of the averages.

	$K_L \to \pi^\pm e^\mp \nu$	$K_L \to \pi^\pm \mu^\mp \nu$	Average
Linear Parametrization ($\times 10^{-3}$)			
λ_+	28.32 ± 0.57	27.45 ± 1.08	28.13 ± 0.51
λ_0		16.57 ± 1.25	16.35 ± 1.21
χ^2/ndf	81.0/65	240.4/236	0.5/1
Quadratic Parametrization ($\times 10^{-3}$)			
λ'_+	21.67 ± 1.99	17.03 ± 3.65	20.64 ± 1.75
λ''_+	2.87 ± 0.78	4.43 ± 1.49	3.20 ± 0.69
λ_0		12.81 ± 1.83	13.72 ± 1.31
χ^2/ndf	62.2/64	230.7/235	1.5/2
Pole Parametrization (MeV/c^2)			
M_v	881.03 ± 7.11	889.19 ± 16.20	882.32 ± 6.54
M_s		1167.14 ± 42.00	1173.80 ± 39.47
χ^2/ndf	66.3/65	234.7/236	0.2/1

inal $\hat{f}_+(t)$ measurement in $K_L \to \pi^\pm e^\mp \nu$, we use a 1-dimensional fit to the $t_\perp^\pi$ distribution performed with fit-A. The choice of $t_\perp^\pi$ over $t_\perp^\ell$ is based on the much smaller sensitivity to radiative corrections (see discussion in Section VI E and Fig. 10). For the nominal $\hat{f}_+(t)$ and $\hat{f}_0(t)$ measurement in $K_L \to \pi^\pm \mu^\mp \nu$, we use a 2-dimensional fit to the $(M_{\pi\mu}, t_\perp^\ell)$ distribution performed with fit-B. The 2-dimensional fit uses the different shape of $\hat{f}_+(t)$ and $\hat{f}_0(t)$ in $M_{\pi\mu}$ (Fig. 6), improving the statistical precision and reducing the correlation between the form factors compared to a 1-dimensional fit to the $t_\perp$ distribution.

The form factor results for the two decay modes and for the three different parameterizations are given in Table II; the correlation coefficients are given in Table III. For all measurements, the statistical and systematic uncertainties are comparable. The $\Delta\chi^2 = 1$ contours for the linear and second order fits based on $K_L \to \pi^\pm \ell^\mp \nu$ decays are shown in Figure 11. The quality of all fits is acceptable. On the other hand, for the $K_L \to \pi^\pm e^\mp \nu$ decay mode, fits to $\hat{f}_+(t)$ using the quadratic and pole parameterizations improve the χ^2 by 18 and 15 units, respectively, compared to the linear parametrization. Taking the systematic uncertainty into account, the significance of the non-linear term in the t dependence of f_+ is about 4σ.

The KTeV result for $\hat{f}_+(t)$ is consistent with a pole model. The fit returns a pole mass $M_v = (882.32 \pm 6.54)$ MeV, in fair agreement with the lightest vector K^* mass (891.66 ± 0.26 MeV).

Lepton universality requires that the $\hat{f}_+(t)$ form factors be equal for the $K_L \to \pi^\pm e^\mp \nu$ and $K_L \to \pi^\pm \mu^\mp \nu$ decay modes. Therefore, we average results for the two decay modes, taking into account statistical and systematic correlations among the parameters, as well as correlation of the systematic uncertainties between the decay modes. The resulting averages are given in the last column of Table II. All parameterizations of $\hat{f}_+(t)$ are consistent for the two decay modes. Note that although the $K_L \to \pi^\pm e^\mp \nu$ decay mode is insensitive to $\hat{f}_0(t)$, the correlation between λ_+ and λ_0 (see Fig. 11) results in an average λ_0 that is different from λ_0 determined only from $K_L \to \pi^\pm \mu^\mp \nu$.

B. Determination of Phase Space Integrals

Using the KTeV average values of the form factors, we calculate the decay phase space integrals (Eq. 8). The results obtained for the three different parameterizations are given in Table IV.

The quadratic parametrization for $\hat{f}_+(t)$ leads to integrals that are about 1% lower than those for the linear parametrization. For our extraction of $|V_{us}|$ [4], we use the quadratic parametrization since the second order term is observed with about 4σ significance.The resulting decay phase space integrals are

$$\begin{aligned} I_K^e &= 0.15350 \pm 0.00044 \pm 0.00095 \\ I_K^\mu &= 0.10165 \pm 0.00039 \pm 0.00070, \end{aligned} \tag{20}$$

where the second error is an additional systematic uncertainty based on the difference between the quadratic and pole models.

C. Crosschecks

We have performed a series of crosschecks on the form factor measurements. A similar set of crosschecks is performed for the linear, quadratic and pole parameterization. Among these tests, the best statistical sensitivity is achieved for the linear fit to λ_+ for $K_L \to \pi^\pm e^\mp \nu$, and for the linear fit to λ_0 with fixed λ_+ for $K_L \to \pi^\pm \mu^\mp \nu$. For simplicity, we report crosschecks using these linear parametrizations.

1. *Consistency among Methods*

As discussed earlier, we determine form factors using both the $t_\perp^\pi$- and $t_\perp^\ell$-methods. For λ_+ measured in the $K_L \to \pi^\pm e^\mp \nu$ decay mode, the difference between the nominal $t_\perp^\pi$-method and the $t_\perp^\ell$-method is $\Delta\lambda_+ = (+0.4 \pm 0.3_{\text{stat}}) \times 10^{-3}$, where the error is the uncorrelated statistical uncertainty estimated using an ensemble of MC samples. Recall from Sec. VI E that without radiative effects in the MC, the $t_\perp^\pi$ and $t_\perp^\ell$ methods disagree by about 20σ. For λ_0 measured in the $K_L \to \pi^\pm \mu^\mp \nu$ decay mode, the difference between the nominal $t_\perp^\ell$-method and the $t_\perp^\pi$-method, $\Delta\lambda_0 = (+0.3 \pm 0.5_{\text{stat}}) \times 10^{-3}$, is also consistent with zero. Similar agreement is observed for the quadratic and pole parameterizations.

Other crosschecks include one- and two-dimensional fits as well as different form factor fitting techniques (fit-A and fit-B) explained in Section V. These crosschecks do not show any systematic biases.

We have checked the $K_L \to \pi^\pm e^\mp \nu$ result using an independent data sample collected with $\times 10$ higher beam intensity. The difference between this analysis and the nominal one is $\Delta\lambda_+ = (-0.3 \pm 0.5_{\text{stat}}) \times 10^{-3}$.

The muon identification in the $K_L \to \pi^\pm \mu^\mp \nu$ decay mode is checked with an analysis in which we do not use the muon system to identify the muon, but instead identify the pion by requiring a hadronic shower in the CsI, which occurs for about 60% of events. The difference between this analysis (which identifies the pion) and the nominal analysis (which identifies the muon) is $\Delta\lambda_0 = (-2.4 \pm 1.5) \times 10^{-3}$. Here, the error is the uncorrelated statistical uncertainty (0.8×10^{-3}), combined with the additional systematic uncertainty arising from the momentum dependent efficiency of the pion identification requirement (1.3×10^{-3}).

TABLE III: a) Total correlation coefficients for $K_L \to \pi^\pm e^\mp \nu$ using quadratic parametrization. For $K_L \to \pi^\pm \mu^\mp \nu$, correlation coefficients are shown for b) linear, c) quadratic, and d) pole parametrizations. For the average of the two $K_L \to \pi^\pm \ell^\mp \nu$ decay modes, correlation coefficients are shown for e) linear, f) quadratic, and g) pole parametrizations.

a)	λ'_+
λ''_+	-0.97

b)	λ_0
λ_+	-0.38

c)	λ_0	λ'_+
λ'_+	0.65	
λ''_+	-0.75	-0.96

d)	M_s
M_v	-0.46

e)	λ_0
λ_+	-0.36

f)	λ_0	λ'_+
λ'_+	0.34	
λ''_+	-0.44	-0.97

g)	M_s
M_v	-0.40

TABLE IV: Phase space integrals for $K_L \to \pi^\pm \ell^\mp \nu$ decays, based on results in Tables II and III.

	I_K^e	I_K^μ
Linear model	0.15507 ± 0.00027	0.10294 ± 0.00026
Quadratic model	0.15350 ± 0.00044	0.10165 ± 0.00039
Pole model	0.15445 ± 0.00023	0.10235 ± 0.00022

2. Consistency among Data Subsets

The stability of the results is tested by dividing the data into subsamples under a variety of criteria. These include decay vertex, minimum track momentum, track separation at the CsI calorimeter, pion-lepton mass, neutrino direction, magnet polarity and lepton charge. All of these checks agree within the uncorrelated statistical uncertainty. A few particularly interesting checks are discussed below.

To verify that the $t_\perp^{\ell,\pi}$-methods are not biased by the ambiguity in the kaon energy, we divide the data into two nearly equal subsamples based on the direction of the neutrino in the kaon rest frame:

$$|\cos\theta_\nu^*| = \sqrt{\frac{{P_{\parallel,\nu}^*}^2}{({P_{\parallel,\nu}^*}^2 + P_{\perp,\nu}^2)}}. \tag{21}$$

For $\cos(\theta_\nu^*) = 0$, the neutrino is emitted perpendicular to the kaon flight direction, and there is only one kaon energy solution; for $|\cos(\theta_\nu^*)| = 1$, the two kaon energy solutions have the maximum difference. The two subsamples for this test are selected by $|\cos(\theta_\nu^*)| < 0.4$, for which the two kaon energy solutions differ on average by 18%, and by $|\cos(\theta_\nu^*)| > 0.4$, for which the two kaon energy solutions differ by 40%. For these two $K_L \to \pi^\pm e^\mp \nu$ samples, we measure $\lambda_+ = (28.0 \pm 0.5_{\rm stat}) \times 10^{-3}$ and $\lambda_+ = (28.9 \pm 0.7_{\rm stat}) \times 10^{-3}$, respectively, showing good agreement. For $K_L \to \pi^\pm \mu^\mp \nu$, there is also good agreement: $\lambda_0(|\cos\theta_\nu^*| < 0.4) - \lambda_0(|\cos\theta_\nu^*| > 0.4) = (1.4 \pm 1.8_{\rm stat}) \times 10^{-3}$.

We check the horizontal alignment of the spectrometer by dividing the $K_L \to \pi^\pm e^\mp \nu$ data into four subsamples based on the lepton charge and the analyzing magnet polarity. This procedure separates the data into classes with tracks bending in different directions in the horizontal plane. We find that for the nominal alignment, the four measurements of λ_+ are consistent ($\chi^2/ndf = 2.95/3$); if the first drift chamber (DC1) is shifted by 50 μm in x-direction, the agreement is significantly worse ($\chi^2/ndf = 30.90/3$). Good agreement is also observed for the same test performed for λ_0 measured in the $K_L \to \pi^\pm \mu^\mp \nu$ decay mode: $\chi^2/ndf = 1.8/3$.

3. Lepton Universality

Lepton universality implies that the coupling constant G_F and the short-distance radiative correction S_{EW} are the same for $K_L \to \pi^\pm e^\mp \nu$ and $K_L \to \pi^\pm \mu^\mp \nu$. Taking the ratio of Eq. 7 for these two modes, we obtain a prediction for the partial width ratio:

$$[\Gamma_{K\mu3}/\Gamma_{Ke3}]_{\rm pred} = \frac{1+\delta_K^\mu}{1+\delta_K^e} \cdot \frac{I_K^\mu}{I_K^e} \ , \tag{22}$$

where the ratio of radiative corrections is calculated to be $(1+\delta_K^\mu)/(1+\delta_K^e) = 1.0058 \pm 0.0010$ [13]. The ratios of the phase space integrals calculated for the linear, quadratic and pole models are:

$$\frac{I_K^\mu}{I_K^e} = \begin{cases} 0.6639 \pm 0.0017 & \text{Linear parametrization} \\ 0.6622 \pm 0.0017 & \text{Quadratic parametrization} \\ 0.6627 \pm 0.0015 & \text{Pole parametrization .} \end{cases} \tag{23}$$

Following the prescription of Sec VII B, we use the quadratic parametrization, and include and additional error based on the pole parametrization to obtain $I_K^\mu/I_K^e = 0.6622 \pm 0.0018$. Using this ratio of the integrals, and the KTeV value of $\Gamma_{K\mu3}/\Gamma_{Ke3}$=0.6640 $\pm$ 0.0014 $\pm$ 0.0022 [16], we obtain

$$\frac{\Gamma_{K\mu3}/\Gamma_{Ke3}}{[\Gamma_{K\mu3}/\Gamma_{Ke3}]_{\rm pred}} = 0.9969 \pm 0.0048 \ , \tag{24}$$

which shows that the KTeV form factors are consistent with the KTeV partial width ratio measurement.

D. Comparison with other Form Factor Measurements

Previous experiments analyzed their data using a linear approximation for $\hat{f}_+(t)$ and $\hat{f}_0(t)$. To compare with these results, we also use the linear parametrization. The comparison of results for λ_+ measured in the $K_L \to \pi^\pm e^\mp \nu$ decay mode is shown in Fig. 12, the λ_+ comparison in $K_L \to \pi^\pm \mu^\mp \nu$ is shown in Fig. 13, and the λ_0 comparison in $K_L \to \pi^\pm \mu^\mp \nu$ is shown in Fig. 14. To simplify the comparison of λ_0, all measurements are adjusted to the same value of $\lambda_+ = 0.030$ using the reported dependences [39].

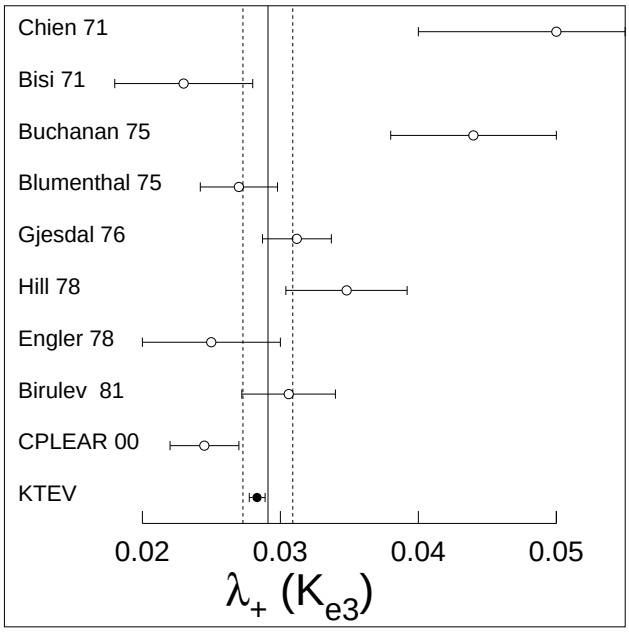

FIG. 12: λ_+ measured in $K_L \to \pi^\pm e^\mp \nu$ decay mode by KTeV and by experiments used in the PDG evaluation (Chien 71 [18], Bisi 71 [19], Buchanan 75 [20], Blumenthal 75 [21], Gjesdal 76 [22], Hill 78 [23], Engler 78 [24], Birulev 81 [25], CPLEAR 00 [6]). The PDG fit (excluding KTeV) is shown by the vertical lines.

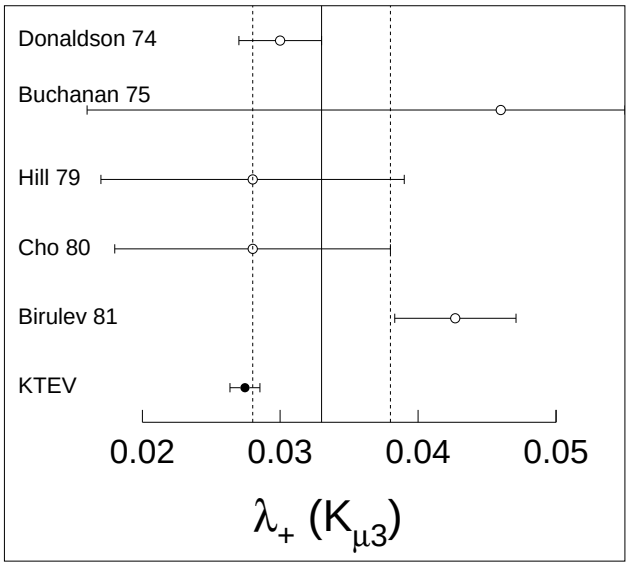

FIG. 13: λ_+ measured in $K_L \to \pi^\pm \mu^\mp \nu$ decay mode by KTeV and by experiments used in the PDG evaluation (Donaldson 74 [26], Buchanan 75 [20], Hill 79 [27], Cho 80 [28], Birulev 81 [25]). The PDG fit (excluding KTeV) is shown by the vertical lines.

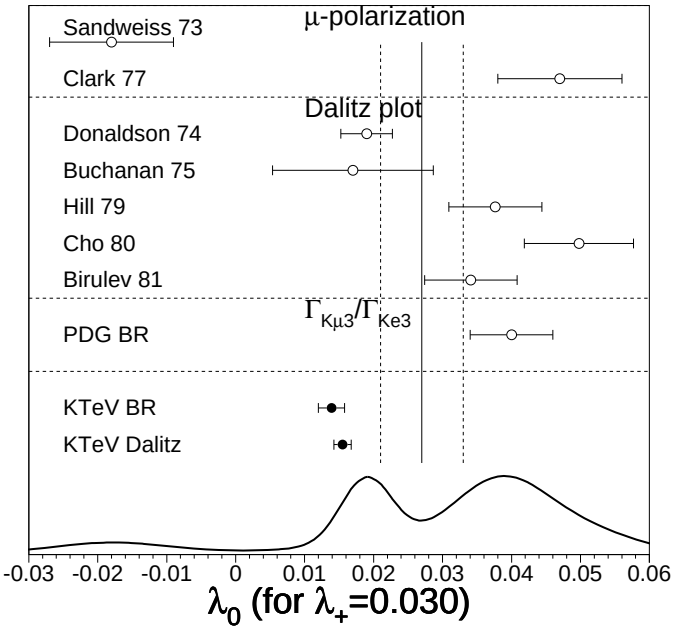

FIG. 14: λ_0 measured by KTeV and by experiments used in the PDG evaluation (Sandweiss 73 [29], Clark 77 [30], Donaldson 74 [26], Buchanan 75 [20], Hill 79 [27], Cho 80 [28], Birulev 81 [25]). PDG BR and KTeV BR are determined using $\Gamma_{K\mu3}/\Gamma_{Ke3}$ and lepton universality. KTeV Dalitz refers to the technique described in this paper. For comparison, all central values and uncertainties are adjusted to $\lambda_+ = 0.030$, using reported dependencies. The PDG fit, based on μ-polarization and Dalitz plot measurements (excluding KTeV result) is shown by the vertical lines. The curve represents a PDG-style ideogram constructed for all but the two KTeV results.

The KTeV λ_+ result for $K_L \to \pi^\pm e^\mp \nu$ is three times more precise than the PDG evaluation; for $K_L \to \pi^\pm \mu^\mp \nu$, our result is almost five times more precise. The new KTeV measurements of λ_+ for both semileptonic decay modes are in agreement with most previous experiments and with the PDG average. The only significant disagreement is between the measurements of λ_+ for $K_L \to \pi^\pm \mu^\mp \nu$ performed by KTeV and Birulev 81 [25]; the difference between these two measurements is more than 3σ (Fig 13).

For λ_0, the experimental situation is less clear (Fig. 14). The KTeV result, which is nearly five times more precise than the PDG evaluation, agrees with only two of the eight previous measurements. Figure 14 also shows a PDG-style ideogram calculated without the KTeV result. This ideogram indicates clustering of the measurements into two groups, one around $\lambda_0 \sim 0.020$ ("middle λ_0 group") and another around $\lambda_0 \sim 0.040$ ("high λ_0 group").

Three different methods have been used to extract λ_0: muon polarization, Dalitz plot density, and $\Gamma_{K\mu3}/\Gamma_{Ke3}$ partial width ratio together with the lepton universality constraint (Eq. 22). The largest inconsistency is a

5σ discrepancy between the two measurements based on muon polarization (Sandweiss 73 [29] and Clark 77 [30]). Sandweiss 73 is the only result with a negative λ_0. The KTeV result does not agree with either of these measurements.

Among the λ_0 measurements based on the Dalitz plot analysis, KTeV agrees well with the highest precision measurement of Donaldson 74 [26], but disagrees with the more recent measurements (Hill 79 [27], Cho 80 [28], Birulev 81 [25]). The largest inconsistency is a 4σ discrepancy between KTeV and Cho 80 [28].

The evaluation of λ_0 from the KTeV measurement of $\Gamma_{K\mu3}/\Gamma_{Ke3}$ agrees with the middle λ_0 group, while the same evaluation based on the PDG fit lands in the high λ_0 group. The PDG value for $\Gamma_{K\mu3}/\Gamma_{Ke3}$ is to a large extent driven by the measurement reported by Cho 80 [28], which disagrees with the analogous KTeV measurement by more than 3σ.

It is worth mentioning that the physics interpretations of the middle and high λ_0 groups are quite different. For the former, the form factors are consistent with a pole model ($\lambda_0 < \lambda_+$), and also agree with those measured for $K^\pm$ [40], suggesting that isospin symmetry breaking effects are small. For the high λ_0 group, where $\lambda_0 > \lambda_+$ (2σ), the simple pole model is disfavoured; the high λ_0 group also shows more than 3σ significance of isospin symmetry breaking for $\hat{f}_0(t)$.

VIII. CONCLUSIONS

In this paper, we have presented new measurements of the form factors in semileptonic K_L decays performed for $K_L \to \pi^\pm e^\mp \nu$ and $K_L \to \pi^\pm \mu^\mp \nu$. The measurement of $\hat{f}_+(t)$ is consistent for the two decay modes, and provides about a threefold increase in precision compared to the PDG average. KTeV measurements of $\hat{f}_+(t)$ are in good agreement with those used in the PDG evaluation.

The KTeV result for λ_0, which is nearly five times more precise than the PDG average, disagrees with six of the eight measurements used in the PDG average. Despite the poor agreement between KTeV and previous results, the most precise measurement [26] used in the PDG evaluation agrees with the KTeV measurement.

The new KTeV result indicates the presence of a non-linear term in the t dependence of f_+ with about 4σ significance. This non-linear term is consistent with pole model expectations. The KTeV result for λ_0 is also consistent with the pole model prediction, and is in agreement with the value measured in $K^\pm$ decays, suggesting that isospin breaking effects are small.

Using the KTeV measurements of the semileptonic form factors, we have calculated the values of the phase space integrals for the $K_L \to \pi^\pm e^\mp \nu$ and $K_L \to \pi^\pm \mu^\mp \nu$ decay modes. We find that inclusion of the non-linear term in the $\hat{f}_+(t)$ expansion reduces the value of these integrals by about 1%. Lepton universality holds for the KTeV data with 0.5% precision, showing consistency between the KTeV form factor measurements presented in this paper, KTeV semileptonic partial width ratios reported in [16], and radiative corrections calculated in [13].

IX. ACKNOWLEDGMENTS

We gratefully acknowledge the support and effort of the Fermilab staff and the technical staffs of the participating institutions for their vital contributions. This work was supported in part by the U.S. Department of Energy, The National Science Foundation, and The Ministry of Education and Science of Japan.

[1] N. Cabibbo, Phys. Rev. Lett. **10**, 531 (1963).
[2] M. Kobayashi and T. Maskawa, Prog. Theor. Phys. **49**, 652 (1973).
[3] H. Leutwyler and M. Roos, Z. Phys. **C25**, 91 (1984).
[4] T. Alexopoulos et al. (KTeV) (2004), submitted to Phys. Rev. Lett., hep-ex/0406001.
[5] Particle Data Group, Phys. Ref. D **66**, 1 (2002).
[6] A. Apostolakis et al., Phys. Lett. **B473**, 186 (2000).
[7] Particle Data Group, Phys. Lett. **111B**, 1 (1982).
[8] H. Battle et al., Phys. Rev. Lett. **73**, 1079 (1994).
[9] G. Abbiendi et al., Eur. Phys. J. C **13**, 213 (2000).
[10] R. Barate et al., Eur. Phys. J. C **10**, 1 (1999).
[11] W. Marciano and A. Sirlin, Phys. Rev. Lett. **56**, 22 (1986).
[12] E. Ginsberg, Phys. Rev. **142**, 1035 (1966).
[13] T. Andre (2004), to be submitted to Phys. Rev. D, hep-ph/0406006.
[14] G. Brandenburg et al., Phys. Rev. **D8**, 1978 (1973).
[15] A. Alavi-Harati et al. (KTeV), Phys. Rev. **D67**, 012005 (2003), hep-ex/0208007.
[16] T. Alexopoulos et al. (KTeV) (2004), submitted to Phys. Rev. D, hep-ex/0406002.
[17] R. Brun et al. (1994), GEANT 3.21, CERN, Geneva.
[18] C. Chien et al., Phys. Lett. **35B**, 261 (1971).
[19] V. Bisi et al., Phys. Lett. **36B**, 533 (1971).
[20] C. Buchanan et al., Phys. Rev. **D11**, 457 (1975).
[21] R. Blumenthal et al., Phys. Rev. Lett. **34**, 164 (1975).
[22] G. Gjesdal et al., Nucl. Phys. **B109**, 118 (1976).
[23] D. Hill et al., Phys. Lett. **73B**, 483 (1978).
[24] A. Engler et al., Phys. Rev. **D18**, 623 (1978).
[25] V. Birulev et al., Nucl. Phys. **B182**, 1 (1981).
[26] G. Donaldson et al., Phys. Rev. **D9**, 2960 (1974).
[27] D. Hill et al., Nucl. Phys. **B153**, 39 (1979).
[28] Y. Cho et al., Phys. Rev. **D22**, 2688 (1980).
[29] J. Sandweiss et al., Phys. Rev. Lett. **30**, 1002 (1973).
[30] A. Clark et al., Phys. Rev. **D15**, 553 (1977).
[31] O. Yushchenko et al., Phys. Lett. **B581**, 31 (2004).
[32] Our notation in this paper is as follows: four-vectors are denoted by P_K, P_π, etc. Spinors are denoted by u_ℓ, u_ν, etc. Three-vectors are given in bold letters. Variables in

the kaon rest frame are denoted by P^*_ν, P^*_π, etc. Components of three-vectors, parallel and perpendicular to the kaon direction are denoted by $p_\perp$ and $p_\parallel$, respectively.

[33] For radiative $K_L \to \pi^\pm \ell^\mp \nu\gamma$ decays we consider diagrams with radiation off the pion, lepton, and hadronic vertex. For radiation off the lepton and vertex, $t = (P_\ell + P_\nu + k)^2 = (P_K - P_\pi)^2$; for radiation off the pion, $t = (P_\ell + P_\nu)^2$.

[34] Our $K_L \to \pi^\pm \mu^\mp \nu$ sample is insufficient to study a second order term in f_0.

[35] A minimum ionising particle deposits about 0.4 GeV in the 50 cm long CsI crystals.

[36] Entries below the diagonal in Fig. 5 (a) and above the diagonal in Fig. 5 (b) fail the condition stated in Eq. 14. These unphysical entries are due to misreconstruction caused by resolution effects and scattering.

[37] Radiative corrections for the t^π distribution are small and depend weakly on the form factors. Radiative corrections therefore can be neglected in the ratio of $F(t_g, \hat{f}_+^{pred}(t_g), \hat{f}_0^{pred}(t_g))$ to $F(t_g, \hat{f}_+^{MC}(t_g), \hat{f}_0^{MC}(t_g))$ if the MC uses form factors which are reasonably close to the true values.

[38] The pion shower requirement is a CsI cluster with energy above 6 GeV; the probability for a muon to satisfy this requirement is less than 0.1%.

[39] Following the PDG prescription, the measurement reported by Birulev 81 [25] has not been adjusted to a different λ_+ value.

[40] The $K^\pm$ form factors from PDG are $\lambda_+(K^+_{e3}) = 0.0283 \pm 0.0015$, $\lambda_+(K^+_{\mu 3}) = 0.033 \pm 0.010$, and $\lambda_0 = 0.013 \pm 0.005$. Recently, the ISTRA+ collaboration reported new measurements of $\lambda_+(K^+_{\mu 3}) = 0.0277 \pm 0.0016$ and $\lambda_0 = 0.0183 \pm 0.0013$ [31].